



High Members of the 2D Ruddlesden-Popper Halide Perovskites: Synthesis, Optical Properties, and Solar Cells of $(\text{CH}_3(\text{CH}_2)_3\text{NH}_3)_2(\text{CH}_3\text{NH}_3)_4\text{Pb}_5\text{I}_{16}$

Constantinos C Stoumpos, Chan Myae Myae Soe, Hsinhan Tsai, Wanyi Nie, Jean-Christophe Blancon, Duyen H Cao, Fangze Liu, Boubacar Traoré, Claudine Katan, Jacky Even, et al.

► To cite this version:

Constantinos C Stoumpos, Chan Myae Myae Soe, Hsinhan Tsai, Wanyi Nie, Jean-Christophe Blancon, et al.. High Members of the 2D Ruddlesden-Popper Halide Perovskites: Synthesis, Optical Properties, and Solar Cells of $(\text{CH}_3(\text{CH}_2)_3\text{NH}_3)_2(\text{CH}_3\text{NH}_3)_4\text{Pb}_5\text{I}_{16}$. Chem, 2017, 2 (3), pp.427-440. 10.1016/j.chempr.2017.02.004 . hal-01486985

HAL Id: hal-01486985

<https://univ-rennes.hal.science/hal-01486985>

Submitted on 31 May 2017

HAL is a multi-disciplinary open access archive for the deposit and dissemination of scientific research documents, whether they are published or not. The documents may come from teaching and research institutions in France or abroad, or from public or private research centers.

L'archive ouverte pluridisciplinaire **HAL**, est destinée au dépôt et à la diffusion de documents scientifiques de niveau recherche, publiés ou non, émanant des établissements d'enseignement et de recherche français ou étrangers, des laboratoires publics ou privés.

High Members of the 2D Ruddlesden-Popper Halide Perovskites: Synthesis, Optical Properties and Solar Cells of $(\text{CH}_3(\text{CH}_2)_3\text{NH}_3)_2(\text{CH}_3\text{NH}_3)_4\text{Pb}_5\text{I}_{16}$

Constantinos C. Stoumpos,¹ Chan Myae Myae Soe,^{1,2} Hsinhan Tsai,^{2,3} Wanyi Nie,² Jean-Christophe Blancon,² Duyen H. Cao,¹ Fangze Liu,² Boubacar Traoré,⁴ Claudine Katan,⁴ Jacky Even,⁵ Aditya Mohite,² Mercouri G. Kanatzidis¹

¹Department of Chemistry, Northwestern University, Evanston, Illinois 60208, USA.

²Los Alamos National Laboratory, Los Alamos, New Mexico 87545, USA.

³Department of Materials Science and Nanoengineering, Rice University, Houston, Texas 77005, USA.

⁴Institut des Sciences Chimiques de Rennes, UMR 6226, CNRS, Université de Rennes 1, 35042 Rennes, France.

⁵FOTON, UMR 6082, INSA de Rennes, CNRS, 35708 Rennes, France.

The Bigger Picture

Ruddlesden-Popper (RP) perovskites are cutting-edge materials in the field of hybrid halide perovskite semiconductors as second-generation systems for optoelectronic devices. We report on the synthesis and characterization of $(\text{CH}_3(\text{CH}_2)_3\text{NH}_3)_2(\text{CH}_3\text{NH}_3)_4\text{Pb}_5\text{I}_{16}$, which represents the fifth ($n = 5$) member of a homologous RP perovskite series. The orthorhombic material has a direct band gap E_g of 1.83 eV and exhibits room-temperature photoluminescence at 678 nm. Density functional theory calculations indicate that the compound has broad electronic bands with light effective masses for electron and hole carriers, comparable with those of the $\text{CH}_3\text{NH}_3\text{PbI}_3$ ($n = \infty$) perovskite, resulting in high charge-carrier mobility required for planar opto-electronic device applications. We thus demonstrate highly stable planar solar cells fabricated with this material as a light absorber with a promising efficiency of 8.71%.

Summary

Here, we present the fifth member ($n = 5$) of the Ruddlesden-Popper $(\text{CH}_3(\text{CH}_2)_3\text{NH}_3)_2(\text{CH}_3\text{NH}_3)_{n-1}\text{Pb}_n\text{I}_{3n+1}$ family, which we successfully synthesized in high yield and purity. Phase purity could be clearly determined from its X-ray powder diffraction patterns, which feature the $(0k0)$ Bragg reflections at low

2 θ angles. The obtained pure $n = 5$ compound was confirmed to be a direct band-gap semiconductor with $E_g = 1.83$ eV. The direct nature of the band gap is supported by density functional theory calculations. Intense photoluminescence was observed at room temperature at 678 nm arising from the band edge of the material. High-quality thin films can be prepared by the hot-casting method from solutions with a pure-phase compound as a precursor. The planar solar cells fabricated with $n = 5$ thin films demonstrate excellent power-conversion efficiency of 8.71% with an impressive open-circuit voltage of ~ 1 V. Our results point to the use of layered perovskites with higher n numbers and pure chemical composition.

Introduction

Halide perovskites are an exciting class of solution-processable semiconductors with a general formula of AMX_3 , where A^+ ($A^+ = Cs$, CH_3NH_3 [MA], or $HC(NH_2)_2$ [FA]) is a small cation that directs the formation of the structure (the “perovskitizer”), M^{2+} is a bivalent p-block metal ion such as Ge, Sn, or Pb, and X^- is a halide ion.^{1, 2, 3, 4, 5, 6} The structure consists of $[MX_{6/2}]^-$ octahedral units, which corner connect to form an extended three-dimensional (3D) framework creating cuboctahedral voids that are occupied by the A^+ cations.⁷ This class of material, particularly $CH_3NH_3PbI_3$, has revolutionized the field of photovoltaics by demonstrating efficiencies of up to 21% within a few years.^{8, 9, 10, 11, 12, 13} Several challenges, however, have come to the fore, one of which concerns the device stability at ambient conditions and their long-term performance.¹⁴

Recently, a soluble semiconductor material system has emerged, namely the lead-based Ruddlesden-Popper (RP) layered perovskites, which promise high performance and exhibit technologically relevant stability.¹⁵ RP perovskites are two-dimensional (2D) materials that derive from the archetypal AMX_3 3D structure by slicing it in a perpendicular direction to a crystallographic plane (typically the (100) plane of the cubic structure) by incorporating the halide salt of a bulky organic spacer. RP perovskites are defined by the general formula $(RNH_3)_2A_{n-1}M_nX_{3n+1}$ (n is an integer between 1 and ∞), where $(RNH_3)^+$ denotes the bulky organic spacer (typically an ammonium cation), which is too large to fit within the perovskite cavity. The layers of $[A_{n-1}M_nX_{3n+1}]$ have a precise thickness that increases with increasing n . This structural architecture, essentially representing a natural multiple quantum well, allows for dielectric confinement, arising from the difference in the dielectric constants ϵ_o and ϵ_i between the organic and inorganic layers, respectively. The quantum confinement begins to diminish as the thickness of $[A_{n-1}M_nX_{3n+1}]$ layers increases with increasing n values, leading to a large and tunable decrease in the optical band gap and the tailoring of their electrical properties.^{16, 17, 18, 19, 20, 21, 22}

To successfully implement 2D RP perovskites in solar cells, one has to control the orientation of the layers so that cross-plane transport occurs in the device. If this is not achieved, the discontinuity of the inorganic perovskite framework that is naturally perpendicular to the layers inhibits the transport of the photo-generated charge carriers. One unexpected feature of these materials is their tendency to orient themselves perpendicular to the

substrate with the layers,²³ and by virtue of a powerful fabrication method called hot-casting,²⁴ it is possible to obtain a nearly perfect orientation of the RP layers perpendicular to the substrate. This enables facile carrier transport across the device, giving power-conversion efficiency of ~12.52%.²⁵ The 2D RP perovskites were found to exhibit superior moisture stability and enhanced durability over their 3D parent compound, most likely because of the formation of a protective layer of the spacer, which does not allow moisture to penetrate and react with the functional semiconducting inorganic layers. However, because the 2D RP perovskites are still a new class of materials that have not been fully developed, they are currently lagging behind 3D perovskites in terms of solar cell performance. In addition, the light absorption is lower because of the relatively wider band gaps of the low-*n* members. Therefore, gaining absorption in the visible region requires investigation of higher-*n*-value members.

Here, we present the fifth member of the $(\text{CH}_3(\text{CH}_2)_3\text{NH}_3)_2(\text{CH}_3\text{NH}_3)_{n-1}\text{Pb}_n\text{I}_{3n+1}$ family, namely $(\text{CH}_3(\text{CH}_2)_3\text{NH}_3)_2(\text{CH}_3\text{NH}_3)_4\text{Pb}_5\text{I}_{16}$ (henceforth termed $\text{BA}_2\text{MA}_4\text{Pb}_5\text{I}_{16}$ or briefly *n* = 5), which we successfully synthesized in high yield and purity. We have determined its crystal structure by using single-crystal X-ray diffraction and have established its optical and electronic properties as well as its utility in the fabrication of solar cells by using the hot-casting method.²⁴

Results and discussion

We achieved the synthesis of $\text{BA}_2\text{MA}_4\text{Pb}_5\text{I}_{16}$ by mixing PbO, MACl, and butylamine (BA) in concentrated aqueous HI (57% w/w) according to the off-stoichiometry protocol to obtain a phase pure material (see Supplemental Information).¹⁵ In this process, BA is used as the limiting reagent in order to prevent fast precipitation, which could lead to crystallization of the less soluble products and a mixture of RP perovskite products. To date, mainly two kinds of RP perovskites have been used in optoelectronic devices: phenylethylammonium (PEA)-based devices, derived from the original work of Calabrese et al.,²⁶ and BA-based devices, derived from the pioneering work of Ishihara et al.¹⁶ on aliphatic ammonium cations, which mostly emphasize the lower-*n* perovskites. In both series of compounds, it has been shown that increasing the number of perovskite layers (*n* in the chemical formula) improves the photovoltaic performance. Specifically, the BA series reaches efficiencies of ~11% for $\text{BA}_2\text{MA}_2\text{Pb}_3\text{I}_{10}$ (*n* = 3) and of ~12% for $\text{BA}_2\text{MA}_3\text{Pb}_4\text{I}_{13}$ (*n* = 4),²⁵ and PEA reaches a maximum efficiency of ~5% for $\text{PEA}_2\text{MA}_2\text{Pb}_3\text{I}_{10}$ (*n* = 3)²⁷ and ~15% for “ $\text{PEA}_2\text{MA}_{59}\text{Pb}_{60}\text{I}_{181}$ (*n* = 60).”²⁸ In the latter case, we use quotation marks because the existence of the *n* = 60 member, which theoretically has a perovskite slab thickness of ~38 nm, has not been documented. It is very likely that such a thickness is above the quantum confinement limit of ~12 nm obtained from work on nanocrystals of the related 3D perovskite CsPbI_3 .²⁹ Although the quality of the devices is excellent, we think that the actual compounds in that work are mainly 3D-like perovskites blended with lower-*n* RP perovskites because the $\text{PEA}_2\text{MA}_2\text{Pb}_3\text{I}_{10}$ (*n* = 3)

member can be clearly identified in most of the X-ray diffraction patterns. Pure RP phases are likely to exist up to the “ $n \sim 10$ ” nominal compositions, as in the case of the oxide RP perovskite phases.³⁰ Thus, we believe the stabilizing effect of PEA does not arise from the formation of RP perovskites but rather as the beneficial effect of additives such as those observed in the purported “ $(5\text{-AVA})_x(\text{MA})_{1-x}\text{PbI}_3$ ” (5-AVA, 5-aminovaleric acid)³¹ and “ $\text{MAPb}(\text{SCN})_2\text{I}$,”³² which were shown to contain mixtures of the RP perovskites $\text{AVA}_2\text{MAPb}_2\text{I}_7$ ($n = 2$)³³ and $\text{MA}_2\text{PbI}_2(\text{SCN})_2$ ($n = 1$), respectively.³⁴ In most of these reports, the absorption spectra seem to contain clear traces of several excitonic features characteristic of the coexistence of various n members, a fact consistent with the forecast that “compounds with $n > 3$ cannot be isolated in a pure form”³⁵ This is mainly because the difference in the thermodynamic stability of the higher- n members is small, and it becomes even smaller as n approaches ∞ , making it difficult to isolate them in pure form. A similar effect is well known for some oxide RP perovskites for which it has been shown that higher- n members tend to disproportionate to the $n = 3$ and $n = \infty$ members by acting as thermodynamic sinks.³⁶ In this work, we demonstrate that the $n = 5$ member can be crystallized in pure form by a specific synthetic procedure.

A single crystal suitable for X-ray diffraction (XRD) was isolated directly from the mother liquor before filtration and mounted on a glass fiber tip. This is a necessary step because the electrostatic nature of the dry crystals and their sensitivity to mechanical deformation hinders the successful selection of single crystals. $\text{BA}_2\text{MA}_4\text{Pb}_5\text{I}_{16}$ crystallizes in an orthorhombic space group with dimensions $a = 8.9050(7) \text{ \AA}$, $b = 77.013(4) \text{ \AA}$, and $c = 8.9313(4) \text{ \AA}$ and incorporates 4 formula units in the unit cell corresponding to two discrete RP layers (Figure 1). The structure of the $n = 5$ compound is a slice that is five $[\text{PbI}_6]^{4-}$ octahedra thick, which share corners along the direction perpendicular to the layers (i.e., the b axis). The individual $[\text{Pb}_5\text{I}_{16}]^{6-}$ slabs are separated by the $(\text{BA}_2)^{2+}$ bilayer with a separation distance of 7.12 \AA . The ordered stacking of the perovskite $[\text{Pb}_5\text{I}_{16}]^{6-}$ layers leads to a large repeating distance of 31.39 \AA for the inorganic moiety within the unit cell, along the stacking direction. Importantly, the raw crystallographic data show the absence of diffuse scattering along the $(0k0)$ direction, indicating the absence of undergrown phases of other n members, further confirming the phase purity of the $n = 5$ RP perovskite (Figure 1C). Guided by our previous work, we have refined the crystal structure as noncentrosymmetric and in the polar space group $C2cb$, which is the expected space group for an odd number of layers (crystallographic information can be found in Tables S1–S5).¹⁵ The structure was refined as an inversion twin, in addition to its “normal” twinning along the (010) axis, with Jana2006.³⁷ For consistency with our previous work, we also report the centrosymmetric version of the structure crystallizing in the *Acam* space group. We select the noncentrosymmetric version on the basis of crystallographic considerations,^{38, 39} but because

the compound is dynamically disordered, one could argue that the centrosymmetric structure represents the average structure, whereas the noncentrosymmetric structure represents a local model in relation to the group-subgroup relationship between the *Acam* (n° 64) and *C2cb* (n° 41) space groups.

To systematically characterize the plate crystals of the pure-phase $n = 5$ compound, we studied the morphology and the crystallography as shown in Figure 2. A pronounced change in the trend of crystal morphology occurred in going from the lower- n members ($n = 1-4$) to the higher- n members ($n > 4$). In the former case, the crystals grew in the form of thin, square, or octagonal platelets and grew freely along the plane of the inorganic layers but only slowly along the vertical stacking direction (Figure 2A). This tendency seemed to weaken for $n = 5$, where in addition to the preferred platelet growth, the crystals exhibited a strong vertical growth habit such that some platelets grew vertically from the existing (010) planes of the thin platelets, leading to extensive twinning (Figure 2). For the $n = 5$ phase, we observed excellent layer formation with high analytical purity with respect to other n members, as demonstrated by high-resolution synchrotron XRD (Figure 2B).

Interestingly, the bulk material showed exceptional stability in humid air in that it maintained its structural integrity for several months; in contrast, bulk MAPbI_3 developed a yellow hue over prolonged periods of time as a result of the formation of the hydrated form, $\text{MAPbI}_3 \cdot \text{H}_2\text{O}$.⁴⁰ The $n = 5$ RP perovskite also showed partial degradation $\text{MAPbI}_3 \cdot \text{H}_2\text{O}$ to , but this was counteracted by the co-formation of the $\text{BA}_2\text{MA}_2\text{Pb}_3\text{I}_{10}$ ($n = 3$) RP perovskite member (Figure S1) according to the following chemical equation:

(Equation 1)



The formation of the $n = 3$ perovskite suggests that the disproportionation mechanism that was discussed above for the oxide RP perovskites³⁶ is also operative in the halide perovskites, in that it offers the added benefit of protecting the perovskite from complete degradation. The disproportionation reaction could be a possible mechanism for the enhanced stability of the RP perovskites. Because the “useless” $\text{MAPbI}_3 \cdot \text{H}_2\text{O}$ is discarded from bulk material, an $n = 3$ RP perovskite “skin” develops, effectively protecting the bulk material from further degradation. Note that the disproportionation of the $n = 5$ perovskite did not produce any black MAPbI_3 perovskite, as attested by the minor MAPbI_3 impurity peaks present in the $n = 5$ sample, which did not evolve over time (see Figure S1). The amount

of MAPbI₃, although relevant to the stability study, was not detectable by any of the optical characterization techniques that are described below.

The high purity of BA₂MA₄Pb₅I₁₆ allows for an accurate determination of the optical properties of the *n* = 5 RP perovskite (Figure 3A). The optical absorption spectrum is characterized by the band edge, an excitonic peak, and an Urbach tail. The band gap of *n* = 5 is estimated to be $E_g = 1.83$ eV after correction for the exciton peak and the Urbach tail. This value agrees well with the band-gap trend whereby the lower-*n* perovskites have values of $E_g = 1.91$ eV (*n* = 4), $E_g = 2.03$ eV (*n* = 3), and $E_g = 2.17$ eV (*n* = 2).¹⁵ Notably, in the present study, the band-gap variation as a function of *n* in RP compounds was pushed beyond *n* = 4, offering further insights into the effects of carrier confinement.⁴¹ The excitonic contribution of *n* = 5 appears only as a kink in the absorption edge, but more detailed spectroscopic studies are needed to quantify its excitonic binding energy.¹⁵ On the other hand, the Urbach tail in *n* = 5 appears to be more pronounced with respect to other lower members, and this could be related to the structural disorder possibly introduced by the extensive twinning or the electronic disorder (trap states) associated with the lowering of the exciton binding energy. Conversely, the photoluminescence (PL) spectrum of *n* = 5 appears to be very well resolved with a near Gaussian-type emission peak at 678 nm. The low-energy tail of the peak is characteristic of the RP perovskites and has been attributed to trap states.⁴² Notably, this low-energy tail is suppressed for the *n* = 5 perovskite with respect to the lower-*n* members, suggesting that the high-*n* members tend to have superior optoelectronic properties. The PL peak, corresponding mainly to the excitonic contribution of the bulk material, agrees well with the experimental band gap, indicating that the confinement effects decrease monotonously with increasing *n*.

To assess the nature of the band gap in BA₂MA₄Pb₅I₁₆ and to better understand the effects of the quantum confinement on the electronic structure of the perovskite, we performed density functional theory (DFT) calculations on the basis of the experimentally determined noncentrosymmetric crystal structure. The electronic band structure of the *n* = 5 RP perovskite with and without spin-orbit coupling (SOC) is shown in Figure 3B. The compound has a direct band gap of $E_g \sim 1.13$ eV without SOC at the Γ point. The conduction band minimum (CBM) is made up of four degenerate states (CBM1–CBM4) followed-up by a 2-fold degenerate state (CBM5 and CBM6) 0.17 eV above, and two nearly degenerate states appear at the top of the valence band (VBM1 and VBM2). The inclusion of SOC into the calculation lifts the degeneracy of the CBM states by about 1 eV, and the band gap is thus lowered to $E_g = 0.28$ eV, still at the Γ point. This is in agreement with the significant role of SOC in hybrid organic-

inorganic iodide perovskites reported in the literature.^{43, 44} It is important to stress that band gaps calculated with plain DFT are underestimated, which is a known issue, and the presented values are only qualitative.^{44, 45} In accordance with earlier findings, the projection of the density of states (DOS) on the different constituent atoms indicates that the top of the valence band (VB) is mainly due to 5p orbitals of I and 6s of Pb, whereas the CBM is mainly due to the 6p states of Pb. The organic molecules have states either too deep in the VB or too high in the conduction band (CB) and do not contribute to VBM or CBM states. In addition, the band structure shows flat dispersions along the Z-T and Y- Γ directions in the reciprocal space, which correspond to layer stacking along the b axis in real space. The flat dispersions indicate the absence of electronic coupling between the inorganic layers along the stacking direction, reflecting the 2D nature of the crystal.

In the energy range of -0.2 to 0.6 eV, several flat dispersion curves are also computed along the Y- Γ line with small energy separation among them for the $n = 5$ perovskite. By comparison, at and close to the band gap, only one band is predicted for the single-layer ($n = 1$) RP perovskite, as well as for the 3D perovskite ($n = \infty$) in both the CB and the VB.^{43, 46} The formation of these flat electronic minibands and the lowering of the band gap for the $n = 5$ RP perovskite are indicative of a systematic vanishing of the quantum confinement effect as n tends to infinity, in agreement with the experimental absorption and emission spectra. However, the prediction of the quantum effect associated with n cannot rely on a simple effective mass Hamiltonian applied to a superlattice built from two bulk materials A and B. The single-layer ($n = 1$) RP perovskite does not contain the atomic motif related to the $A = \text{MAPbI}_3$ material. The limitations of this simple picture and effective mass approaches are clear for small n values supposedly corresponding to ultrathin quantum wells.⁴⁷ The effective mass model with finite confinement predicts unrealistic electronic dispersions in the CB and VB along the stacking axis and minibands that are not predicted by more accurate DFT calculations.⁴⁸ The single-layer ($n = 1$) RP halide perovskite exhibits only one band in the CBM and VBM in the vicinity of the electronic band gap (Figure S2; see also Even et al.⁴³). More generally, the flat dispersion curves in RP phases close to the band gap bear the signatures of a composite material consisting of an inorganic quantum well and an organic barrier with no common Bloch functions between the quantum well and the barrier.^{47, 49} The single CBM and VBM close to the band gap in single-layer RP perovskite are replaced by n CBM and VBM sub-bands (Figure 2B for $n = 5$; for $2 < n < 5$, see Stoumpos et al.¹⁵ and Tsai et al.²⁵). The evanescence of the 2D character of the compound with increasing layer thickness can also be best seen from the comparison between its DOS and those of the $n = 1$ (pure 2D character) and $n = \infty$ (pure 3D character) end members (see Figure S2). This comparison reveals a step-like behavior of the total DOS of the $n = 1$

member near VBM, which is characteristic of a 2D system.⁵⁰ These findings are clearly illustrated in the graphical plots of the Γ point wave functions at VBM and CBM, computed without SOC, in Figure 3C. An unusual feature of these wave functions (ψ) is their appearance at specific octahedral layers for VBM and CBM. ψ_{VBM} is mainly expressed at the “core layers” (second and fourth) with an anti-bonding character between the 5p I orbitals and 6s Pb orbitals, whereas the wave function of CBM (ψ_{CBM}) shows up at the surface layers (first and fifth) and has a bonding character among the 6p lead orbitals. CBM5 and CBM6 (at +0.2 eV), shown in Figure S3, are located on the central layer (third). SOC could possibly interchange the character of these six lowest CBM states but most probably not with even higher lying states (CBM7 at +0.4 eV and CBM8 and CBM9 at +0.6 eV). Thus, the above-mentioned localized character of the VBM and CBM suggests that the electrons and holes are spatially separated within distinct RP perovskite layers. This could prove a useful tool in the engineering of functional devices because it is of great importance regarding the electrical properties of the compounds.

The high-frequency dielectric constant (ϵ_{∞}) profiles were also calculated and are shown in Figure S2 for nanoplatelets of the $n = 1$, $n = 5$, and $n = \infty$ RP perovskites. For the pure 2D compound ($n = 1$), ϵ_{∞} varies from $\epsilon_0 = 2.1$ for the intercalated organic bilayer to $\epsilon_i = 4.0$ for the inorganic perovskite layers. Similarly, the contribution of the organic molecules to ϵ_{∞} remains practically constant ($\epsilon_0 \sim 2.0$) for the $n = 5$ member, given that the number of inorganic layers has little influence on it. However, the contribution of the perovskite thickness to ϵ_{∞} drastically increases to $\epsilon_i = 5.5$ for $n = 5$, effectively reaching the maximum value obtained for the pure 3D end member ($n = \infty$). The calculated values are in reasonable agreement with the experimental ϵ_{∞} values for MAPbI₃, which were measured to be $\epsilon_{\infty} = 3.24$ and $\epsilon_{\infty} = 6.5$ for (C₁₀H₂₁NH₃)₂PbI₄¹⁷ and MAPbI₃,⁵¹ respectively. The increasing ϵ_{∞} in the inorganic part of the compounds as a function of n , i.e., with widening of the inorganic layer, clearly highlights the dielectric confinement effect, which is dominant in the thin layers of the $n = 1$ material but diminishes in $n = 5$ and completely vanishes in the 3D perovskite.^{44, 45} The strong decline of the dielectric confinement in BA₂MA₄Pb₅I₁₆ suggests that the excitonic contribution is smaller in $n = 5$, in good agreement with its absorption spectrum.

Having established the structure and basic material properties of BA₂MA₄Pb₅I₁₆, we proceeded to fabricate solar cells in an initial attempt to evaluate whether the $n = 5$ member is capable of producing working devices, as reported previously for the $n = 3$ and $n = 4$ members;^{23, 25} the solar cell performances are summarized in Figure 4. Using the preformed BA₂MA₄Pb₅I₁₆ bulk material and employing the hot-casting device fabrication protocol,^{24, 25} we succeeded in fabricating preliminary

planar photovoltaic devices with the structure illustrated in Figure 4A. We performed standard solar cell characterization by measuring the current density-voltage (J-V) and external quantum efficiency under illumination as shown in Figures 4B–4D. The light J-V curve for a typical device is plotted in Figure 4B, which shows that the device exhibits a high open-circuit voltage (V_{OC}) of 1.0 V, a short-circuit current density (J_{SC}) of 11.44 mA/cm², and a high fill factor (FF) of 75.59% to yield a power-conversion efficiency of 8.71%. Furthermore, the device made of $n = 5$ does not suffer from hysteresis given that the J-V curves lie on top of each other in scans at different voltage delay times. This suggests that the solar cell figure of merits obtained from J-V characteristics reflects the true performance of the cell.

The statistical values of each parameter are shown in Figure 4C over 20 devices from four different device fabrication batches. The average efficiency achieved is $8.32\% \pm 0.88\%$, featuring a high average $V_{OC} = 0.987 \pm 0.017$ V, $J_{SC} = 11.67 \pm 1.03$ mA/cm², and $FF = 72.12\% \pm 4.07\%$. The external quantum efficiency shown in Figure 4D shows good photocurrent generation in the visible region with a band edge near 790 nm, which is comparable with that of 3D perovskites (Figure S4). The integrated J_{SC} from a typical device is 11.73 mA/cm², which matches well with the value obtained by light J-V curves. The absorption in the near infrared (IR) regime is significantly better than that of the lower- n members of the layered perovskite^{23, 25} because the $n = 5$ member has a thicker inorganic perovskite slab, which gives higher optical absorption. Judging from the relatively low value of external quantum efficiency, we expect the device efficiency to be further improved in the future with further enhancement in J_{SC} . Work in progress addresses this issue and seeks to understand the underlying factors to improve microstructure and thin-film morphology.

We fully demonstrated the structure, purity, and stability of the soluble 2D perovskite semiconductor $(CH_3(CH_2)_3NH_3)_2(CH_3NH_3)_4Pb_5I_{16}$. Combined experimental and theoretical evidence suggest that the higher- n members, starting with $n = 5$, approach the boundaries between the quantum regime of the thin perovskite and the classical bulk materials featuring a ~4-nm-thick perovskite layer. These phenomena have a strong impact on perovskite-based devices because the increasing perovskite thickness helps to achieve higher photocurrents, whereas reduction of the excitonic effects can lead to improved charge collection in devices. The synthesis of higher- n members in pure form is therefore important for identifying the physical limits within which the RP perovskites are stable and exploring the interesting new physics they harbor. Initial solar cells are promising with 8.71% efficiency, and other optoelectronic devices are also possible. Higher- n members of the RP halide perovskites also allow

further tuning of the optical band gap to reach nearly optimum values for perovskite-silicon tandem cells.

Author Contributions

C.C.S., C.M.M.S., and D.H.C. performed the synthesis and characterized the materials. C.C.S. solved the crystal structure and collected and analyzed the X-ray data. H.T., W.N., C.M.M.S., and J.-C.B. fabricated and characterized thin films and devices. B.T., C.K., and J.E. performed DFT calculations. C.K., J.E., A.D.M., and M.G.K. supervised the project. C.C.S. and M.G.K. drafted the manuscript with contributions and edits from all authors.

Acknowledgments

Work at Northwestern University was supported by grant SC0012541 from the US Department of Energy (DOE) Office of Science. Work at Los Alamos National Laboratory (LANL) was supported by the Laboratory Directed Research & Development program. This work was performed in part at the Center for Integrated Nanotechnologies, an Office of Science User Facility operated for the US DOE Office of Science. LANL, an affirmative-action equal-opportunity employer, is operated by Los Alamos National Security for the National Nuclear Security Administration of the US DOE under contract DE-AC52-06NA25396. C.K. and B.T. acknowledge high-performance computing resources from Grand Équipement National de Calcul Intensif (CINES/IDRIS, grant 2016-[x2016097682]). DFT calculations were performed at the Institut des Sciences Chimiques de Rennes, which received funding from the European Union's Horizon 2020 Programme, through a FET Open Research and Innovation under grant 687008. This work made use of the SPID (confocal microscopy) and EPIC (scanning electron microscopy) facilities of Northwestern University's NUANCE Center, which has received support from the Soft and Hybrid Nanotechnology Experimental Resource (NSF ECCS-1542205), the Materials Research Science and Engineering Centers (NSF DMR-1121262), the International Institute for Nanotechnology (IIN), the Keck Foundation, and the State of Illinois through the IIN. Use of the Advanced Photon Source at Argonne National Laboratory was supported by the Basic Energy Sciences program of the US DOE Office of Science under contract DE-AC02-06CH11357.

Figure Captions

Figure 1. The crystal structure of $\text{BA}_2\text{MA}_4\text{Pb}_5\text{I}_{16}$ ($n = 5$). (a) View of the unit cell of the perovskite which includes two individual perovskite layers offset by $\frac{1}{2}$ perovskite cavity length ($\sim 3.15 \text{ \AA}$) normal to the b -axis. (b) View of a single layer along the b -axis highlighting the configuration of the BA and MA cations along the perovskite channels. (c) Precession images generated from the experimental X-ray diffraction data showing the (010) (top) and (101) (bottom) slices of the reciprocal space. The (010) slice is similar

to the ($n = \infty$) perovskite but the (101) slice reveals the crystallographic ordering along the b-axis ((0k0) direction), indicated by the arrows between the ($\bar{2}02$) (blue circle) and ($\bar{2}1\bar{2}2$) (green circle) reflections.

Figure 2. (a) Typical SEM images of $\text{BA}_2\text{MA}_4\text{Pb}_5\text{I}_{16}$ revealing the plate-like morphology of the crystals as well as their tendency towards plastic deformation and vertical twin intergrowth. (b) Synchrotron X-ray powder diffraction pattern (11BM-B, $\lambda = 0.459200 \text{ \AA}$) of a powdered sample of $\text{BA}_2\text{MA}_4\text{Pb}_5\text{I}_{16}$ indicating the high phase purity of the bulk material. Pattern-matching of the data agrees well with the unit cell obtained for the single-crystal. (c) In house X-ray diffraction pattern (Miniflex 600, $\lambda = 1.540593 \text{ \AA}$) on selected individual crystals of $\text{BA}_2\text{MA}_4\text{Pb}_5\text{I}_{16}$ illustrating the tendency of the crystal towards twinning, growing domains normal to the plate-like crystals. As a result, both the (0k0) and ($h0l$) reflections can be observed for a typical crystal as the one shown in the SEM photograph. The scale bars in all SEM images is $50 \mu\text{m}$.

Figure 3. (a) Experimental optical absorption and emission spectra of $\text{BA}_2\text{MA}_4\text{Pb}_5\text{I}_{16}$ ($n = 5$). The spectra of BA_2PbI_4 ($n = 1$), $\text{BA}_2\text{MAPb}_2\text{I}_7$ ($n = 2$), $\text{BA}_2\text{MA}_2\text{Pb}_3\text{I}_{10}$ ($n = 3$), $\text{BA}_2\text{MA}_3\text{Pb}_4\text{I}_{13}$ ($n = 4$), and MAPbI_3 ($n = \infty$) are also shown in the background for comparison purposes. (b) Band structure of $\text{BA}_2\text{MA}_4\text{Pb}_5\text{I}_{16}$ ($Aba2$ space group $\equiv C2cb$; coordinates of high symmetry points are given in Table S6) with and without SOC calculated from the experimental lattice parameters and atomic positions. (c) Γ -point wave functions of $\text{BA}_2\text{MA}_4\text{Pb}_5\text{I}_{16}$ ($n = 5$) at VBM and CBM computed without SOC. The top of VB is mainly composed of 5p orbitals of I and 6s orbitals of Pb while CBM is mainly composed of the empty in-plane 6p states of Pb. The other 2 degenerate states of CBM (CBM3, CBM4, Figure S2) reveal also the in-plane bonding character of Pb 6p orbitals that show up at the 1st and 5th layers of the inorganic part as for CBM1 and CBM2 (CBM5 and CBM6 are given in Figure S3).

Figure 4. Thin Film and Solar Cell Characterization Using $\text{BA}_2\text{MA}_4\text{Pb}_5\text{I}_{16}$ as an Absorbing Layer. (A) Schematic of the planar solar cell architecture used in this study. (B) J-V characteristics for the planar solar cell measured under AM 1.5G illumination. (C) Statistical graph for the solar cell figure of merit for 20 devices. (D) External quantum efficiency (EQE) spectrum for a typical device and the integrated JSC calculated from the EQE on the basis of the solar spectrum.

Figures

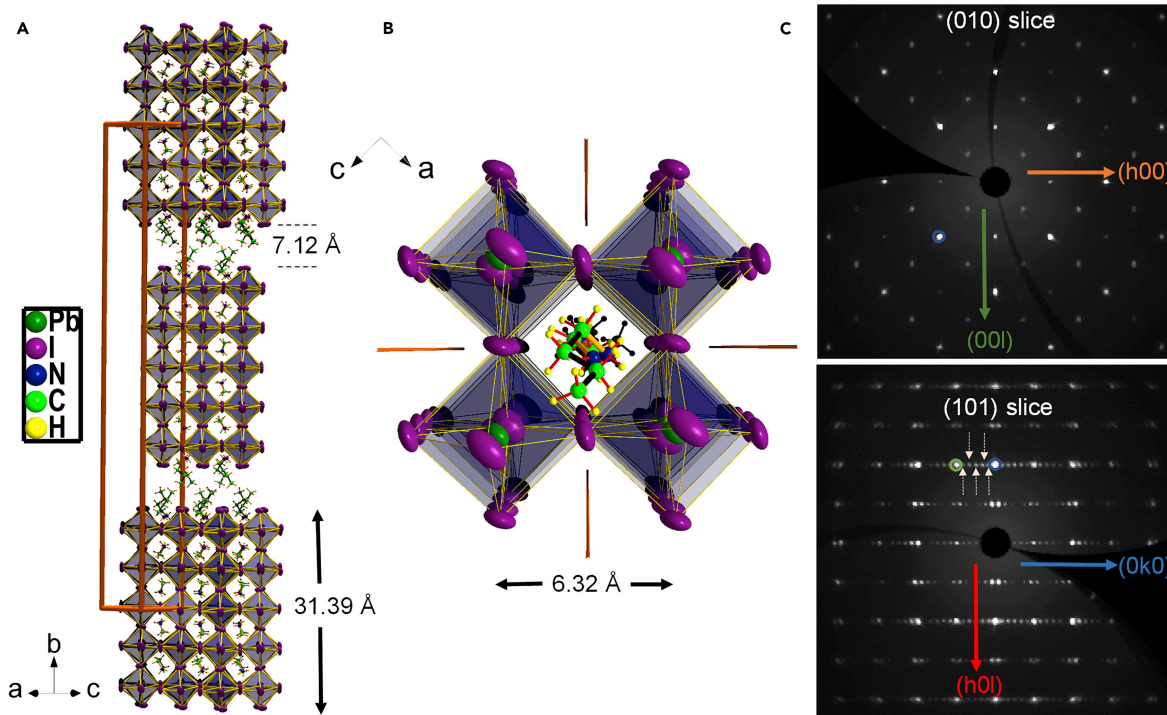


Figure 1

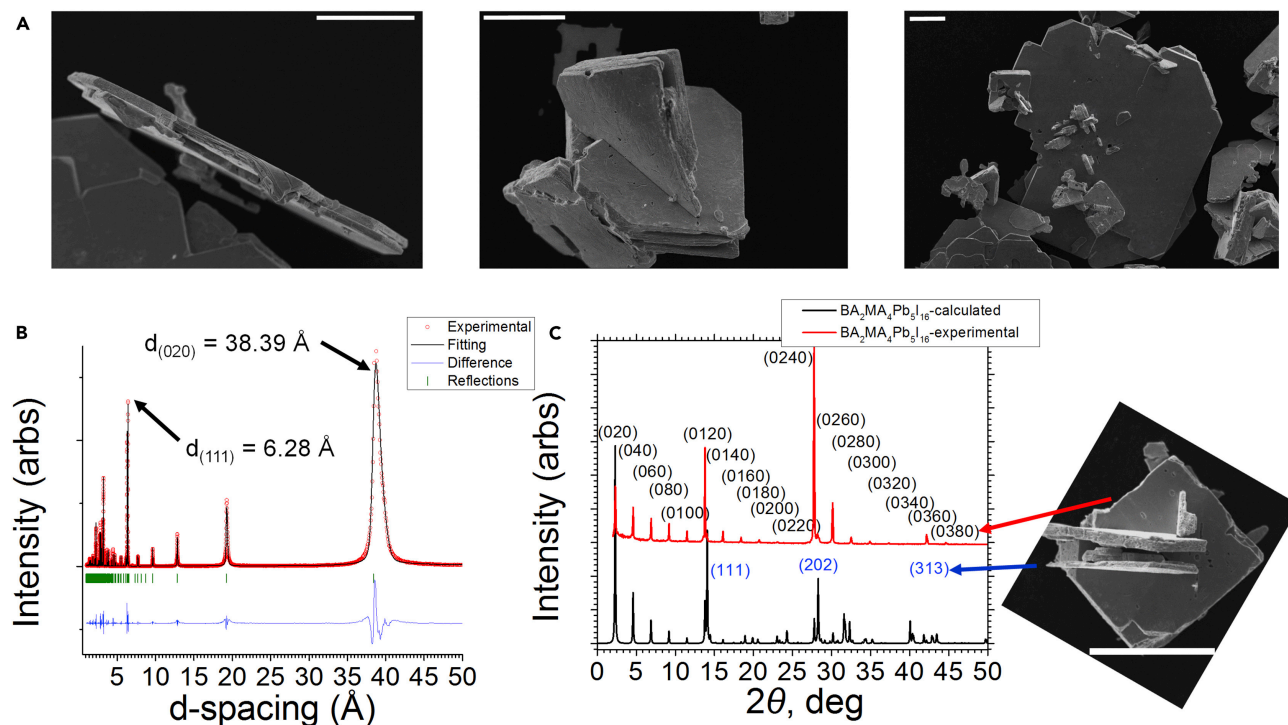


Figure 2

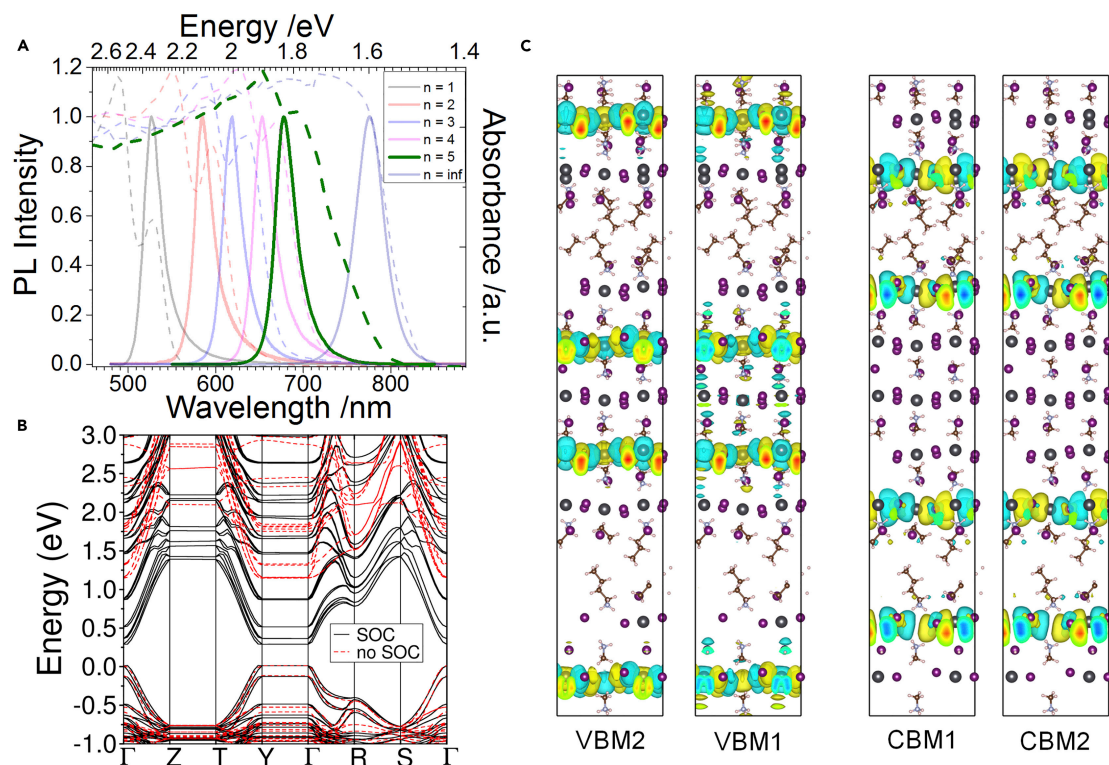


Figure 3

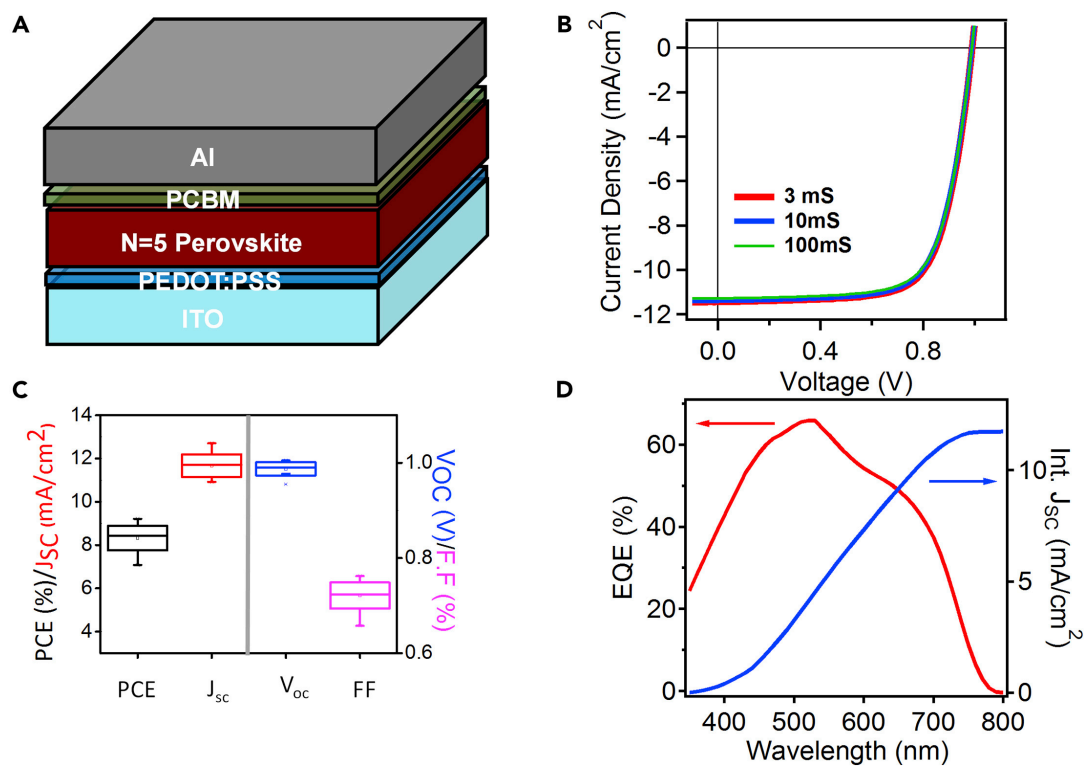


Figure 4

References

1. Stoumpos, C. C.; Kanatzidis, M. G., Halide Perovskites: Poor Man's High-Performance Semiconductors. *Advanced Materials* **2016**, *28* (28), 5778-5793.
2. Saparov, B.; Mitzi, D. B., Organic–Inorganic Perovskites: Structural Versatility for Functional Materials Design. *Chemical Reviews* **2016**, *116* (7), 4558-4596.
3. Manser, J. S.; Christians, J. A.; Kamat, P. V., Intriguing Optoelectronic Properties of Metal Halide Perovskites. *Chemical Reviews* **2016**.
4. Stranks, S. D.; Snaith, H. J., Metal-halide perovskites for photovoltaic and light-emitting devices. *Nat Nano* **2015**, *10* (5), 391-402.
5. Gao, P.; Gratzel, M.; Nazeeruddin, M. K., Organohalide lead perovskites for photovoltaic applications. *Energy & Environmental Science* **2014**, *7* (8), 2448-2463.
6. Boix, P. P.; Agarwala, S.; Koh, T. M.; Mathews, N.; Mhaisalkar, S. G., Perovskite Solar Cells: Beyond Methylammonium Lead Iodide. *The Journal of Physical Chemistry Letters* **2015**, *6* (5), 898-907.
7. Stoumpos, C. C.; Kanatzidis, M. G., The Renaissance of Halide Perovskites and Their Evolution as Emerging Semiconductors. *Accounts of Chemical Research* **2015**, *48* (10), 2791-2802.
8. Kojima, A.; Teshima, K.; Shirai, Y.; Miyasaka, T., Organometal Halide Perovskites as Visible-Light Sensitizers for Photovoltaic Cells. *Journal of the American Chemical Society* **2009**, *131* (17), 6050-6051.
9. Etgar, L.; Gao, P.; Xue, Z.; Peng, Q.; Chandiran, A. K.; Liu, B.; Nazeeruddin, M. K.; Grätzel, M., Mesoscopic CH₃NH₃PbI₃/TiO₂ Heterojunction Solar Cells. *Journal of the American Chemical Society* **2012**, *134* (42), 17396-17399.
10. Kim, H.-S.; Lee, C.-R.; Im, J.-H.; Lee, K.-B.; Moehl, T.; Marchioro, A.; Moon, S.-J.; Humphry-Baker, R.; Yum, J.-H.; Moser, J. E.; Grätzel, M.; Park, N.-G., Lead Iodide Perovskite Sensitized All-Solid-State Submicron Thin Film Mesoscopic Solar Cell with Efficiency Exceeding 9%. *Scientific Reports* **2012**, *2*, 591.
11. Lee, M. M.; Teuscher, J.; Miyasaka, T.; Murakami, T. N.; Snaith, H. J., Efficient Hybrid Solar Cells Based on Meso-Superstructured Organometal Halide Perovskites. *Science* **2012**, *338* (6107), 643-647.
12. Jeon, N. J.; Noh, J. H.; Yang, W. S.; Kim, Y. C.; Ryu, S.; Seo, J.; Seok, S. I., Compositional Engineering of Perovskite Materials for High-Performance Solar Cells. *Nature* **2015**, *517* (7535), 476-480.
13. Yang, W. S.; Noh, J. H.; Jeon, N. J.; Kim, Y. C.; Ryu, S.; Seo, J.; Seok, S. I., High-Performance Photovoltaic Perovskite Layers Fabricated Through Intramolecular Exchange. *Science* **2015**, *348* (6240), 1234-1237.
14. Niu, G.; Guo, X.; Wang, L., Review of Recent Progress in Chemical Stability of Perovskite Solar Cells. *Journal of Materials Chemistry A* **2015**, *3* (17), 8970-8980.
15. Stoumpos, C. C.; Cao, D. H.; Clark, D. J.; Young, J.; Rondinelli, J. M.; Jang, J. I.; Hupp, J. T.; Kanatzidis, M. G., Ruddlesden–Popper Hybrid Lead Iodide Perovskite 2D Homologous Semiconductors. *Chemistry of Materials* **2016**, *28* (8), 2852-2867.
16. Ishihara, T.; Takahashi, J.; Goto, T., Exciton-State in Two-Dimensional Perovskite Semiconductor (C₁₀H₂₁NH₃)₂PbI₄. *Solid State Communications* **1989**, *69* (9), 933-936.
17. Hong, X.; Ishihara, T.; Nurmikko, A. V., Dielectric Confinement Effect on Excitons in PbI₄-Based Layered Semiconductors. *Physical Review B* **1992**, *45* (12), 6961-6964.
18. Papavassiliou, G. C.; Koutselas, I. B., Structural, Optical and Related Properties of Some Natural Three- and Lower-Dimensional Semiconductor Systems. *Synthetic Metals* **1995**, *71* (1–3), 1713-1714.
19. Koutselas, I. B.; Ducasse, L.; Papavassiliou, G. C., Electronic Properties of Three- and Low-Dimensional Semiconducting Materials with Pb Halide and Sn Halide Units. *Journal of Physics: Condensed Matter* **1996**, *8* (9), 1217-1227.

20. Tanaka, K.; Takahashi, T.; Kondo, T.; Umebayashi, T.; Asai, K.; Ema, K., Image Charge Effect on Two-Dimensional Excitons in an Inorganic-Organic Quantum-Well Crystal. *Physical Review B* **2005**, *71* (4), 045312.
21. Yaffe, O.; Chernikov, A.; Norman, Z. M.; Zhong, Y.; Velauthapillai, A.; van der Zande, A.; Owen, J. S.; Heinz, T. F., Excitons in Ultrathin Organic-Inorganic Perovskite Crystals. *Physical Review B* **2015**, *92* (4), 045414.
22. Mitzi, D. B.; Feild, C. A.; Harrison, W. T. A.; Guloy, A. M., Conducting Tin Halides with a Layered Organic-Based Perovskite Structure. *Nature* **1994**, *369* (6480), 467-469.
23. Cao, D.H., Stoumpos, C.C., Farha, O.K., Hupp, J.T., and Kanatzidis, M.G. 2D homologous perovskites as light-absorbing materials for solar cell applications. *J. Am. Chem. Soc.* **2015**; *137*: 7843–7850
24. Nie, W.; Tsai, H.; Asadpour, R.; Blancon, J.-C.; Neukirch, A. J.; Gupta, G.; Crochet, J. J.; Chhowalla, M.; Tretiak, S.; Alam, M. A.; Wang, H.-L.; Mohite, A. D., High-efficiency solution-processed perovskite solar cells with millimeter-scale grains. *Science* **2015**, *347* (6221), 522-525.
25. Tsai, H.; Nie, W.; Blancon, J.-C.; Stoumpos, C. C.; Asadpour, R.; Harutyunyan, B.; Neukirch, A. J.; Verduzco, R.; Crochet, J. J.; Tretiak, S.; Pedesseau, L.; Even, J.; Alam, M. A.; Gupta, G.; Lou, J.; Ajayan, P. M.; Bedzyk, M. J.; Kanatzidis, M. G.; Mohite, A. D., High-efficiency two-dimensional Ruddlesden–Popper perovskite solar cells. *Nature* **2016**, *536* (7616), 312-316.
26. Calabrese, J.; Jones, N. L.; Harlow, R. L.; Herron, N.; Thorn, D. L.; Wang, Y., Preparation and Characterization of Layered Lead Halide Compounds. *Journal of the American Chemical Society* **1991**, *113* (6), 2328-2330.
27. Smith, I. C.; Hoke, E. T.; Solis-Ibarra, D.; McGehee, M. D.; Karunadasa, H. I., A Layered Hybrid Perovskite Solar-Cell Absorber with Enhanced Moisture Stability. *Angewandte Chemie International Edition* **2014**, *53* (42), 11232-11235.
28. Quan, L. N.; Yuan, M.; Comin, R.; Voznyy, O.; Beauregard, E. M.; Hoogland, S.; Buin, A.; Kirmani, A. R.; Zhao, K.; Amassian, A.; Kim, D. H.; Sargent, E. H., Ligand-Stabilized Reduced-Dimensionality Perovskites. *Journal of the American Chemical Society* **2016**, *138* (8), 2649-2655.
29. Protesescu, L.; Yakunin, S.; Bodnarchuk, M. I.; Krieg, F.; Caputo, R.; Hendon, C. H.; Yang, R. X.; Walsh, A.; Kovalenko, M. V., Nanocrystals of Cesium Lead Halide Perovskites (CsPbX₃, X = Cl, Br, and I): Novel Optoelectronic Materials Showing Bright Emission with Wide Color Gamut. *Nano letters* **2015**, *15* (6), 3692-3696.
30. Lee, C.-H.; Podraza, N.J.; Zhu, Y.; Berger, R.F.; Shen, S.; Sestak, M.; Collins, R.W.; Kourkoutis, L.F.; Mundy, J.A.; Wang, H. et al. Effect of reduced dimensionality on the optical band gap of SrTiO₃. *Appl. Phys. Lett.* **2013**; *102*: 122901
31. Mei, A.; Li, X.; Liu, L.; Ku, Z.; Liu, T.; Rong, Y.; Xu, M.; Hu, M.; Chen, J.; Yang, Y.; Grätzel, M.; Han, H., A hole-conductor-free, fully printable mesoscopic perovskite solar cell with high stability. *Science* **2014**, *345* (6194), 295-298.
32. Jiang, Q.; Rebollar, D.; Gong, J.; Piacentino, E. L.; Zheng, C.; Xu, T., Pseudohalide-Induced Moisture Tolerance in Perovskite CH₃NH₃Pb(SCN)₂I Thin Films. *Angewandte Chemie International Edition* **2015**, *54* (26), 7617-7620.
33. Mercier, N., (HO₂C(CH₂)₃NH₃)₂(CH₃NH₃)Pb₂I₇: a Predicted Non-Centrosymmetrical Structure Built up from Carboxylic Acid Supramolecular Synthons and Bilayer Perovskite Sheets. *CrystEngComm* **2005**, *7* (70), 429-432.
34. Daub, M.; Hillebrecht, H., Synthesis, Single-Crystal Structure and Characterization of (CH₃NH₃)₂Pb(SCN)₂I₂. *Angewandte Chemie* **2015**, *127* (38), 11168-11169.
35. Papavassiliou, G. C., Three- and Low-Dimensional Inorganic Semiconductors. *Prog Solid State Ch* **1997**, *25* (3-4), 125-270.

36. Yan, L.; Niu, H. J.; Duong, G. V.; Suchomel, M. R.; Bacsa, J.; Chalker, P. R.; Hadermann, J.; van Tendeloo, G.; Rosseinsky, M. J., Cation ordering within the perovskite block of a six-layer Ruddlesden-Popper oxide from layer-by-layer growth - artificial interfaces in complex unit cells. *Chemical Science* **2011**, 2 (2), 261-272.
37. Petříček, V.; Dušek, M.; Palatinus, L., Crystallographic Computing System JANA2006: General features. *Zeitschrift für Kristallographie - Crystalline Materials* **2014**, 229 (5), 345.
38. Hamilton, W., Significance Tests on the Crystallographic R Factor. *Acta Crystallographica* **1965**, 18 (3), 502-510.
39. Rogers, D., On the Application of Hamilton's Ratio Test to the Assignment of Absolute Configuration and an Alternative Test. *Acta Crystallographica Section A* **1981**, 37 (5), 734-741.
40. Hao, F.; Stoumpos, C.C.; Liu, Z.; Chang, R.P.H., and Kanatzidis, M.G. Controllable perovskite crystallization at a gas-solid interface for hole conductor-free solar cells with steady power conversion efficiency over 10%. *J. Am. Chem. Soc.* 2014; 136: 16411–16419
41. Tanaka, K. and Kondo, T. Bandgap and exciton binding energies in lead-iodide-based natural quantum-well crystals. *Sci. Tech. Adv. Mater.* 2003; 4: 599–604
42. Wu, X.; Trinh, M. T.; Niesner, D.; Zhu, H.; Norman, Z.; Owen, J. S.; Yaffe, O.; Kudisch, B. J.; Zhu, X. Y., Trap States in Lead Iodide Perovskites. *Journal of the American Chemical Society* **2015**, 137 (5), 2089-2096.
43. Even, J.; Pedesseau, L.; Dupertuis, M. A.; Jancu, J. M.; Katan, C., Electronic model for self-assembled hybrid organic/perovskite semiconductors: Reverse band edge electronic states ordering and spin-orbit coupling. *Physical Review B* **2012**, 86 (20), 205301.
44. Even, J.; Pedesseau, L.; Jancu, J.-M.; Katan, C., Importance of Spin–Orbit Coupling in Hybrid Organic/Inorganic Perovskites for Photovoltaic Applications. *The Journal of Physical Chemistry Letters* **2013**, 4 (17), 2999-3005.
45. Katan, C.; Pedesseau, L.; Kepenekian, M.; Rolland, A.; Even, J., Interplay of spin-orbit coupling and lattice distortion in metal substituted 3D tri-chloride hybrid perovskites. *Journal of Materials Chemistry A* **2015**, 3 (17), 9232-9240.
46. Pedesseau, L.; Jancu, J.-M.; Rolland, A.; Deleporte, E.; Katan, C.; Even, J., Electronic properties of 2D and 3D hybrid organic/inorganic perovskites for optoelectronic and photovoltaic applications. *Optical and Quantum Electronics* **2014**, 46 (10), 1225-1232.
47. Even, J.; Pedesseau, L.; Katan, C., Understanding Quantum Confinement of Charge Carriers in Layered 2D Hybrid Perovskites. *ChemPhysChem* **2014**, 15 (17), 3733-3741.
48. Akkerman, Q.A.; Motti, S.G.; Srimath Kandada, A.R.; Mosconi, E.; D’Innocenzo, V.; Bertoni, G.; Marras, S.; Kamino, B.A.; Miranda, L.; De Angelis, F. et al. Solution synthesis approach to colloidal cesium lead halide perovskite nanoplatelets with monolayer-level thickness control. *J. Am. Chem. Soc.* 2016; 138: 1010–1016
49. Even, J.; Pedesseau, L.; Katan, C.; Kepenekian, M.; Lauret, J.-S.; Saponi, D.; Deleporte, E., Solid-State Physics Perspective on Hybrid Perovskite Semiconductors. *The Journal of Physical Chemistry C* **2015**, 119 (19), 10161-10177.
50. Chuang, S.L. *Physics of Photonic Devices*. John Wiley, ; 2009
51. Hirasawa, M.; Ishihara, T.; Goto, T.; Uchida, K.; Miura, N., Magnetoabsorption of the lowest exciton in perovskite-type compound (CH₃NH₃)PbI₃. *Physica B: Condensed Matter* **1994**, 201, 427-430.
52. Toby, B. CMPR - a powder diffraction toolkit. *J. Appl. Crystallogr.* 2005; 38: 1040–1041
53. Axtell, E. A.; Liao, J. H.; Pikramenou, Z.; Kanatzidis, M. G., Dimensional Reduction in II-VI Materials: A₂Cd₃Q₄ (A=K, Q=S, Se, Te; A=Rb, Q=S, Se), Novel Ternary Low-Dimensional Cadmium Chalcogenides Produced by Incorporation of A₂Q in CdQ. *Chem-Eur J* **1996**, 2 (6), 656-666.

54. Chondroudis, K.; McCarthy, T. J.; Kanatzidis, M. G., Chemistry in Molten Alkali Metal Polyselenophosphate Fluxes. Influence of Flux Composition on Dimensionality. Layers and Chains in APbPSe_4 , $\text{A}_4\text{Pb}(\text{PSe}_4)_2$ ($\text{A} = \text{Rb}, \text{Cs}$), and $\text{K}_4\text{Eu}(\text{PSe}_4)_2$. *Inorganic Chemistry* **1996**, *35* (4), 840-844.
55. Hohenberg, P.; Kohn, W., Inhomogeneous Electron Gas. *Physical Review* **1964**, *136* (3B), B864-B871.
56. Kohn, W.; Sham, L. J., Self-Consistent Equations Including Exchange and Correlation Effects. *Physical Review* **1965**, *140* (4A), A1133-A1138.
57. José, M. S.; Emilio, A.; Julian, D. G.; Alberto, G.; Javier, J.; Pablo, O.; Daniel, S.-P., The SIESTA method for ab initio order- N materials simulation. *Journal of Physics: Condensed Matter* **2002**, *14* (11), 2745.
58. Perdew, J. P.; Burke, K.; Ernzerhof, M., Generalized Gradient Approximation Made Simple. *Physical Review Letters* **1996**, *77* (18), 3865-3868.
59. Troullier, N.; Martins, J. L., Efficient pseudopotentials for plane-wave calculations. *Physical Review B* **1991**, *43* (3), 1993-2006.
60. Billing, D. G.; Lemmerer, A., Synthesis, Characterization and Phase Transitions of the Inorganic-Organic Layered Perovskite-Type Hybrids $[(\text{C}_n\text{H}_{2n+1}\text{NH}_3)_2\text{PbI}_4]$ ($n = 12, 14, 16$ and 18). *New Journal of Chemistry* **2008**, *32* (10), 1736-1746.
61. Baikie, T.; Fang, Y.; Kadro, J. M.; Schreyer, M.; Wei, F.; Mhaisalkar, S. G.; Graetzel, M.; White, T. J., Synthesis and crystal chemistry of the hybrid perovskite $(\text{CH}_3\text{NH}_3)\text{PbI}_3$ for solid-state sensitised solar cell applications. *Journal of Materials Chemistry A* **2013**, *1* (18), 5628-5641.
62. Kawamura, Y.; Mashiyama, H.; Hasebe, K., Structural Study on Cubic–Tetragonal Transition of $\text{CH}_3\text{NH}_3\text{PbI}_3$. *J Phys Soc Jpn* **2002**, *71* (7), 1694-1697.
63. Even, J.; Pedesseau, L.; Kepenekian, M., Electronic surface states and dielectric self-energy profiles in colloidal nanoscale platelets of CdSe . *Physical Chemistry Chemical Physics* **2014**, *16* (45), 25182-25190.
64. Saponi, D.; Kepenekian, M.; Pedesseau, L.; Katan, C.; Even, J., Quantum confinement and dielectric profiles of colloidal nanoplatelets of halide inorganic and hybrid organic-inorganic perovskites. *Nanoscale* **2016**, *8* (12), 6369-6378.